Elastic-Beam Triboelectric Nanogenerator for High-Performance Multifunctional Applications: Sensitive Scale, Acceleration/Force/Vibration Sensor, and Intelligent Keyboard

Yuliang Chen, Yi-Cheng Wang, Ying Zhang, Haiyang Zou, Zhiming Lin, Guobin Zhang, Chongwen Zou, and Zhong Lin Wang*

Exploiting novel devices for either collecting energy or self-powered sensors is vital for Internet of Things, sensor networks, and big data. Triboelectric nanogenerators (TENGs) have been proved as an effective solution for both energy harvesting and self-powered sensing. The traditional triboelectric nanogenerators are usually based on four modes: contact-separation mode, lateral sliding mode, single-electrode mode, and freestanding triboelectric-layer mode. Since the reciprocating displacement/force is necessary for all working modes, developing efficient elastic TENG is going to be important and urgent. Here, a kind of elastic-beam TENG with arc-stainless steel foil is developed, whose structure is quite simple, and its working states depend on the contact area and separating distance as proved by experiments and theoretical calculations. This structure is different from traditional structures, e.g., direct sliding or contact-separation structures, whose working states mainly depend on contact area or separating distance. This triboelectric nanogenerator shows advanced mechanical and electrical performance, such as high sensitivity, elasticity, and ultrahigh frequency response, which encourage applications as a force sensor, sensitivity scale, acceleration sensor, vibration sensor, and intelligent keyboard.

1. Introduction

With the rapid development of Internet of Things and sensor network over the past decades, enormous electronic devices such as sensors, transmitters, and actuators have been used all over the world. Each device requires a small power (in microwatt to milliwatt range) for operation; however, providing persistent power sources for such electronics remains challenging. Therefore, the exploration for self-powered sensors and energy harvesting techniques has turned into one of the best alternatives for the new era—the era of Internet of Things.[1–3]

On the other hand, mechanical energy is ubiquitous in the ambient environment, such as vibration, breeze, and water wave. If the energy can be converted into electrical output, it could become sustainable power sources to meet the lower power requirement of various sensors. In 2012, Dr. Zhong Lin Wang's group first proposed an emerging technique called triboelectric nanogenerator (TENG) that can efficiently convert mechanical energy from the ambient environment into electrical output, taking advantage of contact-electrification and electrostatic induction.[4] The converted electrical signals can then be used as power sources or sensor signals. For example, the mechanical energy of ocean waves, human motions, wind, and even raindrop can be converted to electrical energy based on various types of TENGs.[5–9] In addition, the self-powered sensors based on TENGs have been successfully applied to motion, vibration, environmental, and biological monitoring.[10–15]

There are four basic operation modes for TENGs.[16] Among those modes, contact-separation and sliding are two foremost and fundamental principles, both depend on the motions between two dissimilar materials.[17–22] The working principles of the former depend mainly on the separated distance between two dissimilar materials, since the area of the two materials are

Y. L. Chen, Dr. Y.-C. Wang, Prof. Y. Zhang, H. Y. Zou, Z. M. Lin,
Prof. Z. L. Wang
School of Materials Science and Engineering
Georgia Institute of Technology
Atlanta, GA 30332-0245, USA
E-mail: zhong.wang@mse.gatech.edu
Y. L. Chen, Prof. G. B. Zhang, Prof. C. W. Zou
National Synchrotron Radiation Laboratory
University of Science and Technology of China
Hefei 230029, China

Prof. Z. L. Wang
Beijing Institute of Nanoenergy and Nanosystems
Chinese Academy of Sciences
Beijing 100083, China
Prof. Z. L. Wang
College of Nanoscience and Technology
University of Chinese Academy of Sciences
Beijing 100049, China

**ADVANCED
SCIENCE NEWS**
www.advancedsciencenews.com

**ADVANCED
ENERGY
MATERIALS**
www.advenergymat.de

generally fixed.[18,19] For the sliding mode, its working principle is mainly associated with the contacted area of two dissimilar materials, since there is no vertical separation between the two materials.[20,23] However, sliding fraction may lead to low durability of the TENGs and the most of the induced charges are transferring at the moment of contacting or separating between the two materials.[18,19,24,25] In addition, in order to continuously harvesting mechanical energy or using TENGs as self-powered sensors, it is very critical for a TENG to recover to its original state automatically after the mechanical motion was removed. Researchers have applied spring or elastic polymers to deal with this problem;[11,26–29] however, those methods could increase the complexity of the device fabrication that may prevent them from mass production.

To address this issue and further improve the performance of TENGs, herein, we integrated an elastic-beam (EB) arc-stainless steel foil (arc-SSF) into the TENG structure and developed a novel EB-TENG. According to our experimental, theoretical, and numerical results, the working principles of the EB-TENG depend not only on the area of contact but also on the separation distance between the arc-SSF and dielectric layer of the EB-TENG.[14] In addition, after the contact event was removed, e.g., releasing the pressed SSF, the system could recover to its original state automatically owing to the elasticity of SSF. We also showed that the electrical output of the designed EB-TENG is highly sensitive to external force and can provide excellent response at high-frequency. By virtue of the structural design and material properties, we further demonstrated that this EB-TENG can be used as force sensor, sensitive scale, acceleration sensor, vibration sensor, or smart keyboard. We believe this novel design of the EB-TENG with arc-SSF can be generalized to other TENGs that can further improve the performance of energy harvesting and self-powered sensors.

2. Results and Discussion

2.1. Structural Design and Working Principle of EB-TENG

Figure 1a is the schematic of EB-TENG based on arc-SSF. A copper (Cu) film and a polytetrafluoroethylene (PTFE) film were pasted on an acrylic (polymethyl methacrylate, PMMA) board successively. Then, one end of an arc-SSF was fixed on the PTFE/Cu/PMMA structure to complete the fabrication of EB-TENG. The width and length of the EB-TENG are 7.5 and 60 mm, respectively. Other details of the fabrication processes are presented in the Experimental Section. Figure 1b shows the photo of the EB-TENG device. Two wires were connected to the SSF and the copper film with the conjunctions winded by Kapton tape. The length of EB-TENG can be adjusted by a black rubber ring (Figure S1a, Supporting Information). The working principle of the EB-TENG at open-circuit condition is summarized as follows (Figure 1c). After the first contact-separation

event happens between SSF and PTFE triggered by mechanical force, I) the SSF becomes positively charged and the PTFE becomes negatively charged, based on the triboelectric series.[30] II) These triboelectric charges (Q) stay on both SSF and PTFE, due to the open-circuit condition (for SSF) and the dielectric properties of the PTFE layer. Pressing the SSF would not change the amount of triboelectric charge but change the capacitance of EB-TENG (C), which is affected by increasing the contacted area (A) and separated distance (h) between the SSF and the PTFE. The open-circuit voltage (U) is inversely proportional to C. Hence, U would change when pressing the SSF. III) When the SSF is fully contacted with the PTFE, the A reaches maximum and h to minimum. IV) Releasing the SSF to recover A and h partially. Finally, the SSF moves back to initial position to complete a cycle. The defined variables are listed in Table S1 in the Supporting Information.

2.2. Performance Characterization, Theoretical Calculation, and Finite Element Analysis (FEA)

To take advantage of the structural design and further apply the EB-TENG to other applications, it is necessary to test the mechanical behaviors and the electrical output of the EB-TENG. **Figure 2**a shows the experimental setup: an analytical balance was placed beneath the EB-TENG and was used to record the external force (F); an oscilloscope was used to measure the open-circuit voltage U. The height (h) is defined as the vertical distance from the vertex of the SSF to the PTFE. The displacement (d) is defined as the variation of h, $d = h_0 - h$, where h_0 is the initial height of the vertex of SSF. When pressed the SSF, the h was then reduced (d increased), and we can get the corresponding U, F, and d (Figure 2b). Intuitively, the relationships of U versus F, U versus d, and F versus d are illustrated in Figure 2c,e and Figure S2 in the Supporting Information, respectively. Figure 2b and Figure S2 in the Supporting Information display that the last point is beyond the range of measurement. Therefore, we did not plot the last point in Figure 2c,e, which indicates that the U increases with increasing F and d. In addition, it should be
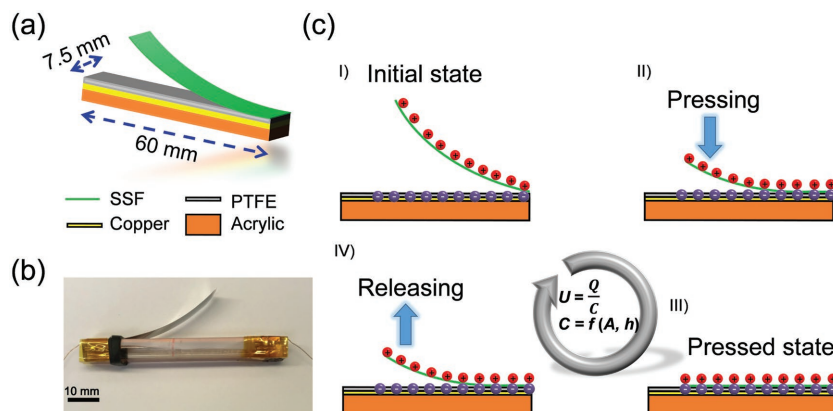

Figure 1. a) The schematic of the elastic-beam triboelectric nanogenerator (EB-TENG). b) The picture of the actual EB-TENG device. A black rubber ring is used to adjust the length of EB-TENG. c) The working principle at open-circuit condition. The output of EB-TENG depends on the contact area and separation distance between the SSF and the PTFE.
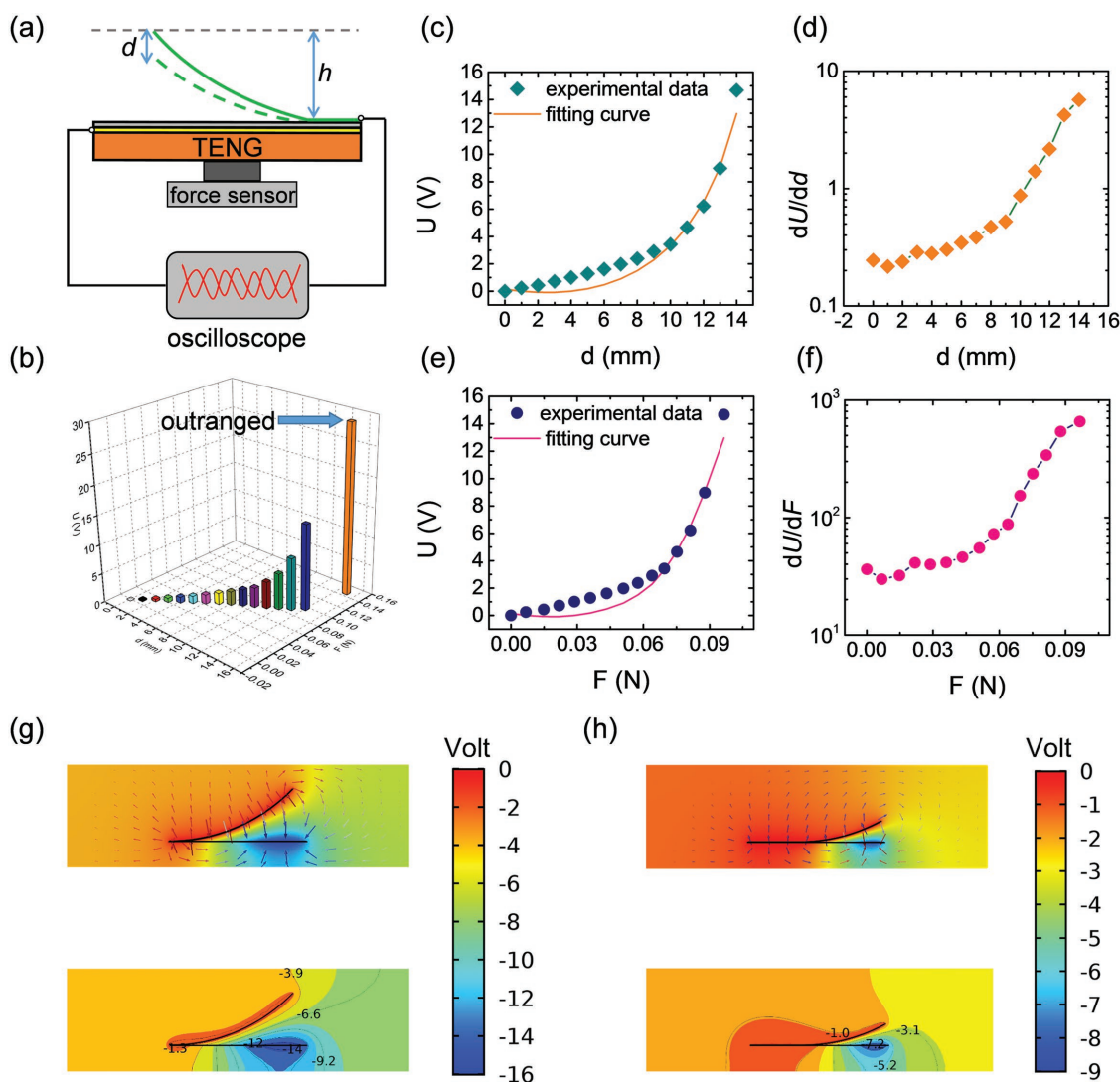
Figure 2. a) The experimental setup: an analytical balance is placed beneath the EB-TENG and is used to record the F applied; an oscilloscope used to record the U. b) The experimental results of U versus d and F. c) The results of U versus d, the experimental data and fitting data indicated by olive diamond and orange curve, respectively. And the corresponding differential curve in (d). e) The U versus F, the experimental data and fitting data indicated by navy dot and pink curve, respectively. And the corresponding differential curve in (f). g) The potential distribution of the initial state of the EB-TENG under open-circuit condition. h) The potential distribution of the partially pressed state of the EB-TENG under open-circuit condition.

pointed out that the relationships of U versus F and U versus d are not linear in Figure 2e,c, which is different from the results of the regular contact-separation TENGs in ideal plane-parallel capacitor mode,[18] showing linear relationships. Figure S3a in the Supporting Information shows the standard deviation of U with increasing d from independent measurements and one of the measurements shows in Figure S3b in the Supporting Information. Figure S1b in the Supporting Information shows the experimental results of U versus d and F after reducing the length of SSF by moving the rubber ring.

In order to further understand the working mechanism of the EB-TENG, we conducted theoretical calculation and FEA. In previous reports, the open-circuit voltage U of TENGs is always associated with contacted area and separated distance between two dissimilar materials.[18,20,31,32] For our device, the width of SSF is fixed at 7.5 mm, so the contacted area (A) between the SSF

and PTFE is proportional to the length (l) of the contacted part of SSF. The separated distance between the vertex of SSF and PTFE could be presented as h, since the SSF has a symmetrical shape. Moreover, $d = h_0 - h$, hypothesized the U can be written as follows

$$U = k_1 l + k_2 d + k_3 \tag{1}$$

where k_1, k_2, and k_3 are fitting parameters; k_3 is introduced as a constant that includes other factors, such as the roughness of friction layers, edge effect. The fitting results can be described as follows

$$U = -158 \arcsin\left(\frac{\sqrt{15.16 - \dfrac{F}{0.00678}}}{10}\right) - 351.03F + 63.34 \tag{2}$$

ADVANCED
SCIENCE NEWS
www.advancedsciencenews.com

ADVANCED
ENERGY
MATERIALS
www.advenergymat.de

$$U = -158 \arcsin\left(\sqrt{\frac{15.16-d}{100}}\right) - 2.38d + 63.34 \qquad (3)$$

It can be found that the nonlinearity for $U(F)$ and $U(d)$ attributing to the antitrigonometric functions in Equations (2) and (3). The fitting results are plotted in Figure 2c,e with each corresponding measured data. The detail derivation is described in Note S1 in the Supporting Information.

Figure 2g is the potential distribution of the initial state under open-circuit condition by FEA. The colors correspond to the magnitude of potential. In the top panel of Figure 2g, it indicates a higher potential for SSF and a lower potential for PTFE as expected due to the negative charges transferred from SSF to PTFE after contacting (followed by separating event). The arrows show the electric field lines. Their directions from high potential to low potential match the potential distribution. Interestingly, we found the electric field lines are perpendicular to the surface of SSF, whereas they are inclined to the surface of PTFE. As we known, SSF is a conductor and PTFE is an insulator, which means SSF is an equipotential body and PTFE is not. So there is no electric field component along the surface of SSF. The equipotential lines in the bottom part of Figure 2g verify the speculation, i.e., the potential of the right part of PTFE is lower than that of the left part. Similar results can be found in the partially pressed state (Figure 2h), whose potential difference (U) is reduced compared to initial state, which matches our experimental results in Figure 2c,e. It should be noted that the SSF was connected to the ground in our experimental setup. And the potential difference U of the initial state was set to the baseline. This is the reason that U increasing with larger F (Figure 2e) and d (Figure 2c).

2.3. Sensitive Scale and Acceleration Sensor

Figure 2f shows the differential curve of dU versus dF, which could be used to estimate the sensitivity of EB-TENG. It suggests the sensitivity dU/dF is about 30–900 V N^{-1}. The calculated sensitivity dU/dd can be up to maximum $\approx$6 N mm^{-1} in Figure 2d. The high sensitivity suggests the excellent performance of the EB-TENG (the higher sensitivity can be achieved by changing the fabrication of EB-TENG, e.g., the wider SSF applied). To further take advantage of this property, we then applied the EB-TENG as a scale. In Figure 3a, two same screws (each is 0.9350 g) were weighed by using EB-TENG. The measured values derived from the relationship of U versus F are 0.932 ± 0.04 g for single screw

and 1.867 ± 0.03 g for two screws, which is well accordant with the actual values. In practical scenarios, we usually want to weigh the mass to an expected value. In the up panel of Figure 3b, we increased the mass to the expected value (8 g) step by step. And the below panel of Figure 3b shows the scenario of increasing and reducing mass randomly. For these two scenarios, the tested data well match the actual results, which demonstrate great performance in our EB-TENG. According to the results in Figure 2e, the corresponding range of measured mass is 0–9.85 g for the present EB-TENG. The wider measured range can be achieved by applying high Young's modulus SSF in similar structure of EB-TENG.
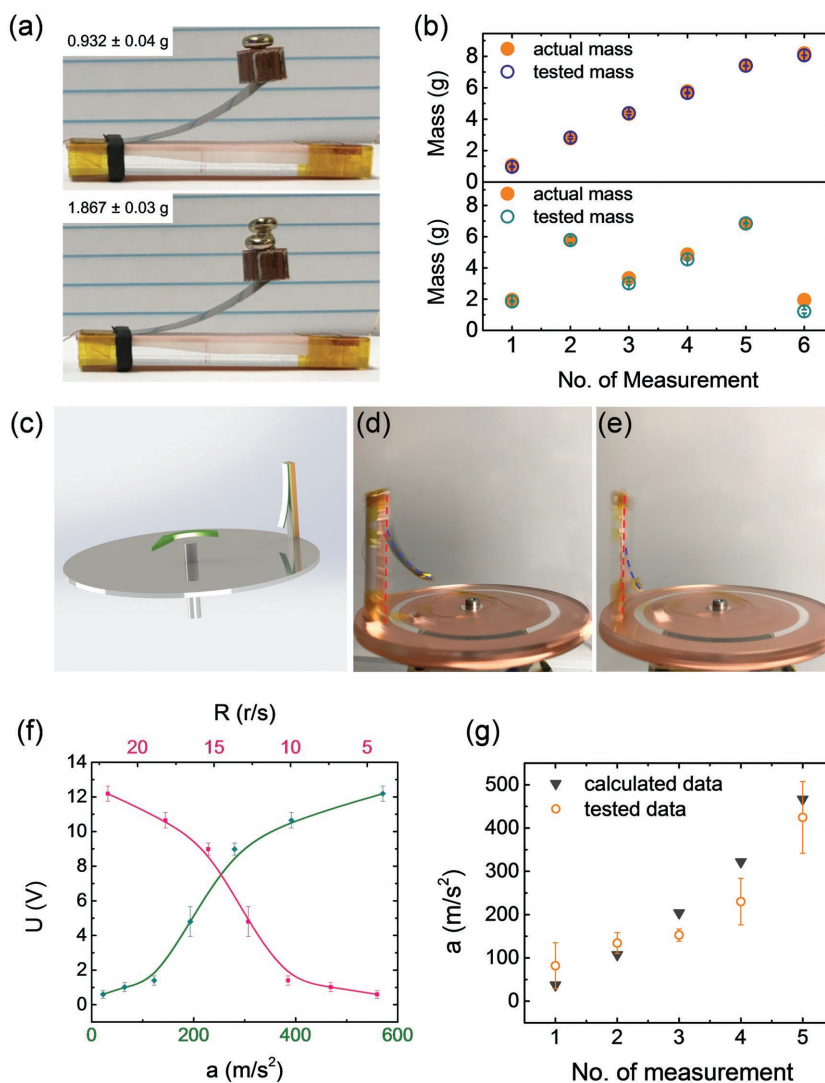

Figure 3. a) Two identical screws are put onto the tip of the SSF and weighed by the EB-TENG. b) The two different situations of weighing. The up panel shows weighing mass to the expected value step-by-step. The bottom part shows increasing and decreasing mass randomly during the weighing process. c) The schematic for the EB-TENG as an acceleration sensor. The EB-TENG is fixed on a disk and could spin with the disk. The actual picture of the EB-TENG spinning d) at low revolving speed and e) at high revolving speed. The red dashed line shows the PTFE and the blue dashed line shows the arc-SSF. A tiny 0.4 g weight is fixed at the vertex of SSF. f) The experimental results of U versus revolving speed (R) and acceleration (a). g) The calculated acceleration (gray triangle) and the tested acceleration by EB-TENG (orange circle). The error bars represent standard deviation from independent measurements.

**ADVANCED
SCIENCE NEWS**

www.advancedsciencenews.com

**ADVANCED
ENERGY
MATERIALS**

www.advenergymat.de

According to above discussion, the fabricated EB-TENG definitely can be used as a force sensor. Based on $F = ma$, m is mass and a denotes acceleration, if set a at a constant value, the EB-TENG can be used to measure m as discussed in last section ($a = g$, where g is gravitational acceleration and treated as a constant value). On the other hand, if set m at a constant value, the EB-TENG can be used as an acceleration sensor.

As Figure 3c shown, an EB-TENG is fixed at the edge of a disk. Then the combined structure was installed on a rotary motor. The EB-TENG would subject to different centrifugal forces when the disk was spinning at different speeds, in another word, the different acceleration can be applied on the EB-TENG in terms of only a same 0.4 g weight fixed at the vertex of SSF. When the revolving speed (R) was fast (Figure 3e), the pressed degree was deeper than that of the pressed state at slow revolving speed (Figure 3d). Figure 3f shows the measured results of U versus R (pink curve) and a (olive curve) when the EB-TENG was put on a radius (r) 30 mm disk, which indicates faster R or bigger a would bring greater U. Figure S4 in the Supporting Information shows one of the measurements, U versus time at different R. These relationships are accordant to the positive correlation of U versus F in Figure 2e. Furthermore, in order to test the performance of the EB-TENG, it was fixed on another radius 50 mm disk. In Figure 3g, the measured data derived from the relationship of a and U in Figure 3f can well match the calculated acceleration (by formula $v^2/r = (2\pi rR)^2/r$, where v is speed), and the inconformity between them could attribute to the influence of wind when the disk was spinning. The influence of wind could be avoided, for example, packaging the EB-TENG in a box.

2.4. Frequency Simulation and Vibration Sensor

Furthermore, we checked the frequency performance of EB-TENG. Taken a fixed shape to consider, the eigenfrequency (or resonant frequency) $f \propto \sqrt{E/\rho}$, where E notes Young's modulus and ρ is density.[33] For usual elastic materials, such as rubber, the typical value of E is in the range of $\approx 10^6$ Pa. However, the E of SSF is about five orders of magnitude higher (in $\approx 10^{11}$ Pa range). More importantly, the densities of SSF and rubber are generally in the same order of magnitude ($\approx 10^3$ kg m^{-3}). This result implies that our SSF-based EB-TENG could have a better performance at high-frequency. **Figure 4**a shows the relationship of eigenfrequency versus the noncontacting arc length of SSF by FEA, which suggests the eigenfrequency can be from 53 to 85 279 Hz when the length varies from 40 to 1 mm. The eigenfrequency values of the SSF are almost two orders of magnitude higher than that of rubber (Figure S5, Supporting Information, details in Note S2, Supporting Information). Figure 4b is the simulated results for 40 mm arc length (initial state) operated at the eigenfrequency, which shows the vertex has a bigger displacement from the color mapping (Figure S6, Supporting Information). Similar results for 20 mm arc length are displayed in Figure S7 in the Supporting Information.

To apply our theoretical analysis and simulation results, we conducted an additional set of experiments. The vertex of
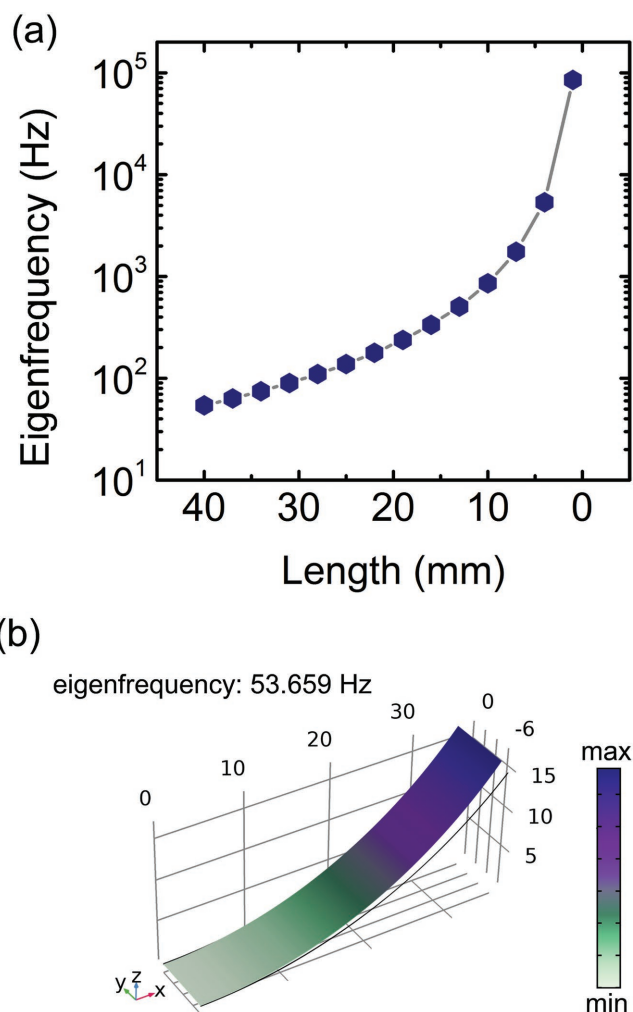

Figure 4. a) The simulated results of eigenfrequency versus the uncontacting arc length of SSF. b) The simulated results for 40 mm arc length (initial state) working at the eigenfrequency. The color displays the displacement distribution of each position qualitatively.

the SSF on the EB-TENG was set to contact with a vibrator as shown in **Figure 5**e. The signals were input into the vibrator to drive the EB-TENG. The measured signals by EB-TENG can be obtained by an oscilloscope or played by a loudspeaker through an amplifier. Figure 5a–d shows the measured voltage signals by EB-TENG when the sine waves at different frequencies were input into the vibrator (more results in Figure S8, Supporting Information). Compared to the background noise (the initial small signals in Figure 5a–d), the detected signals are quite prominent with high signal-to-noise ratio even up to ultrahigh frequency (e.g., 18 kHz). The amplitude of voltage decreasing with time in Figure 5b, Figure S8b in the Supporting Information, and increasing in Figure 5d probably originate from the measuring instrument rather than the EB-TENG. When a commercial vibration sensor was adopted to measure the voltage signal at 1 kHz under the same conditions, the results show the same decreasing trend as shown in Figure S9 in the Supporting Information. The frequencies that can be heard by human being are between 20 Hz and 20 kHz. Then, we input
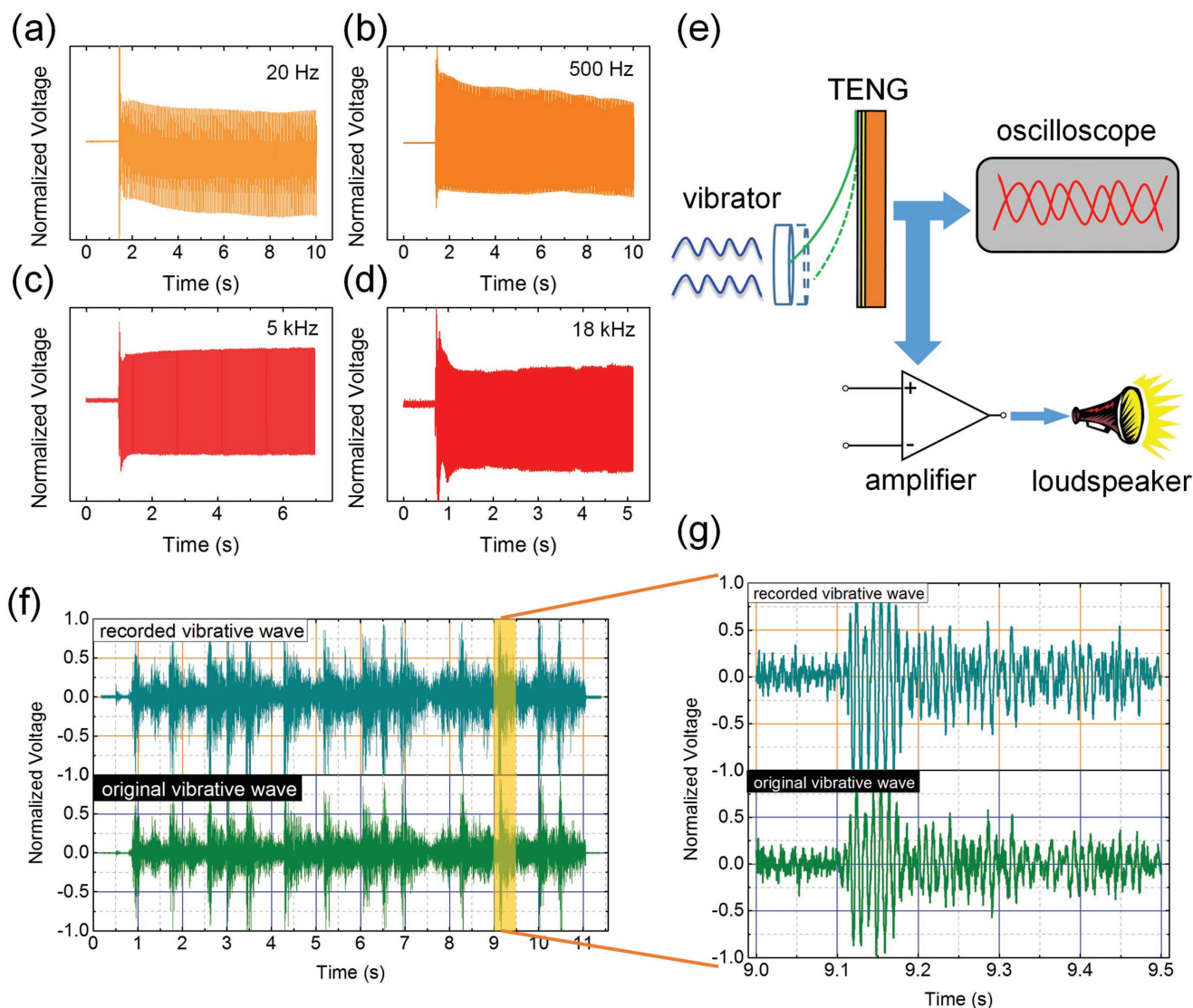
Figure 5. a–d) The measured voltage signals by EB-TENG at different frequencies. e) The experimental setup of the frequency response for EB-TENG. f) A piece of music input to a vibrator. The up panel shows the detected wave by EB-TENG. The bottom panel shows the original wave. The detailed comparison between original results and detected results by EB-TENG is presented in (g).

a piece of music into the vibrator, and the detected results are demonstrated in Figure 5f,g. Compared to the original signals, the recorded signals show a good accordance (Figure S10, Supporting Information), which can be used to generate an audio file (Audio S1, Supporting Information). In this audio, the different sounds of instruments can be distinguished, such as drum, trombone.

2.5. Intelligent Keyboard Application

For traditional keyboards, the method of input is based on the on/off states of each switch (unit), corresponding to 1 and 0, respectively, as shown in **Figure 6**a. Before the switch is connected, the all states of switch only represent 0. However, in the big data and artificial intelligence (AI) era, an intelligent keyboard that can provide additional information is highly desired.[28] Herein,

we developed a multiple states input devices (MSIDs) based on EB-TENG, taking advantage of the successive voltage variation of the pressed states (Figure 6b). The inset of Figure 6b shows the fabricated numeric keyboard integrating numbers from 1 to 9 (the fabricated details in the Experimental Section). First, we tested the on/off performance for individual key. In Figure 6c, two binary sequences based on Morse code (Table S2, Supporting Information) were input to express "SOS" and "911", respectively. The on/off states can be switched sharply, which suggests the fabricated EB-TENG keyboard is compatible with the function of traditional keyboards. Then a numeric sequence "298 157 436" was input randomly with different pressing force. In Figure 6d, it can be observed that the input magnitudes of numbers are different, which can achieve the function of MSIDs. For instance, in Figure 6e, the "3" has the largest magnitude and "1" has the smallest magnitude. The magnitudes can carry additional information in numerous practical
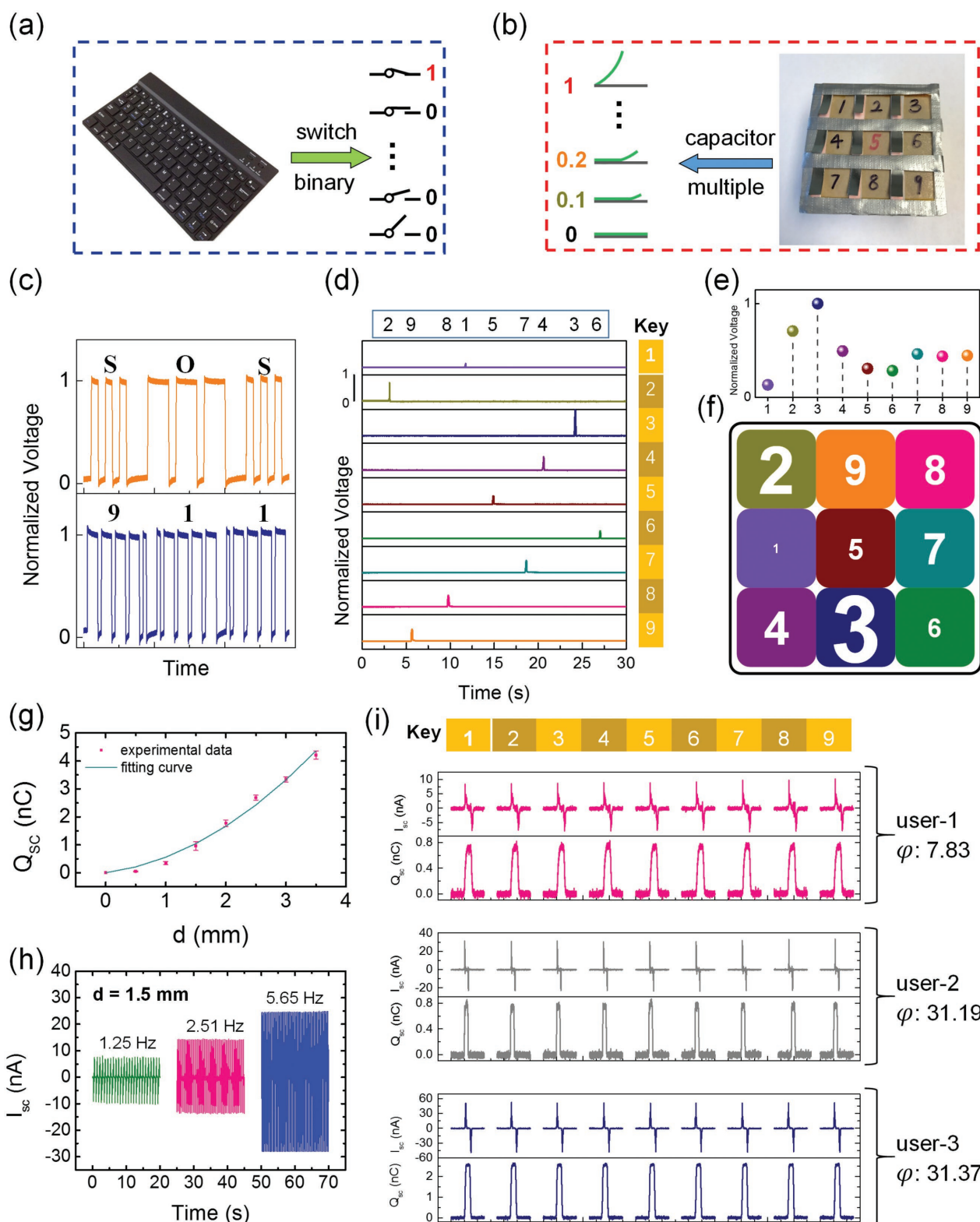
Figure 6. a) A traditional keyboard based on on/off switch that only has binary states. b) A smart keyboard based on EB-TENG that can have multiples states. c) Two binary sequences based on Morse code were input to express "SOS" and "911" by EB-TENG keyboard. d) A numeric sequence input by EB-TENG keyboard with different signal magnitudes due to different pressing forces. e) The extracted normalized magnitude of the voltage output from (d). f) The numbers in different size, which is proportional to the extracted normalized magnitude of the voltage output. g) The measured and fitting results of transferred short-circuit charge (Q_{sc}) versus d. h) The short-circuit current (I_{sc}) of periodic pressing SSF ($d = 1.5$ mm) at different typing frequencies. i) Three typical typing results for indicating the basic principle of keystroke dynamics by EB-TENG keyboard.

**ADVANCED
SCIENCE NEWS**

www.advancedsciencenews.com

**ADVANCED
ENERGY
MATERIALS**

www.advenergymat.de

applications. For example, if we want characters with different sizes, we can set the size of the characters to be proportional to the electrical output magnitude. Figure 6f shows the numeric sequence with different sizes, based on different output magnitudes.

Based on people's typing attributes, keystroke dynamics as a kind of unconditioned reflex, for example, the typing force and typing speed, can be utilized as the "fingerprint" to develop personal identity verification, cyber security, and AI technology.[34–36] Here, the short-circuit condition was applied to our EB-TENG and the short-circuit working processes are specified in Figure S11 in the Supporting Information. We found that the transferred short-circuit charge (Q_{sc}) and short-circuit current (I_{sc}) can reflect the vital information of keystroke dynamics. Taken individual key of EB-TENG keyboard to consider, the increase of Q_{sc} accompanies the more forceful pressing due to the short-circuit working condition (Figure 6g), which implies the information of typing force. The fitting equation of Q_{sc} versus d (olive curve in Figure 6g) is

$$Q_{sc} = 0.275d^2 + 0.282d \tag{4}$$

When the pressing state keeps constant ($d = 1.5$ mm), the higher typing frequency produces bigger I_{sc} as Figure 6h shown (more results based on other d and frequencies in Figure S12, Supporting Information), which can be explained by formula $I_{sc} = dQ_{sc}/dt$, in a shorter time (t) to obtain a certain Q_{sc}, the bigger I_{sc} would be generated. Moreover, three typical examples are presented to expound the basic principle of keystroke dynamics by EB-TENG keyboard in Figure 6i. Compared the results between user 1 and user 2, the Q_{sc} are almost same, which means that the two users have near the same typing force. However, the amplitude of I_{sc} of user 2 is almost four times that of user 1. Obviously, user 2 is typing faster than user 1. The Q_{sc} of user 3 is more than that of other users, so user 3 has the biggest typing force in the three users. Although the amplitude of I_{sc} of user 3 is highest, the typing speed of user 3 is difficult to directly compare with other users through I_{sc} because the bigger I_{sc} of user 3 could originate from the increased amount of Q_{sc} or faster typing speed. In order to exclude the influence of increased amount of Q_{sc}, a parameter φ was introduced

$$\varphi = \frac{I_{scm}}{\dfrac{dQ_{sc}}{dd}} \tag{5}$$

where I_{scm} is the amplitude of I_{sc}. According to Equations (4) and (5), the calculated φ are 7.83, 31.19, and 31.37 for these three users, respectively. With these results, in fact, user 3 has near typing speed to user 2 even if user 3 has the biggest typing force. The more discussion is in Note S3 in the Supporting Information.

3. Conclusion

In this work, we fabricated a novel EB-TENG based on SSF. The structure of EB-TENG is quite simple, and its working states depend on the contact area and separation distance proved by our experiments and theoretical calculation, which is different from traditional structures, for example, contact-separation mode depending on the separation distance and sliding mode depending on the contact area. Moreover, we developed this EB-TENG to be used as a force sensor, sensitive scale, acceleration sensor, vibration sensor, and intelligent keyboard, which all showed good performance. This novel structure of EB-TENG with arc-SSF can be applied to other TENGs as devices of collecting energy and self-powered sensor in future.

4. Experimental Section

Fabrication of the EB-TENG: A 7.5 mm × 60 mm × 5 mm acrylic board was used as the substrate. First, a copper film as an electrode was pasted on the top of the acrylic board. Then, the PTFE (with 0.127 mm thickness) was pasted on top of the copper film. The SSF (Alfa Aesar, type 304, width of 7.5 mm, arc length of 45 mm, thickness of 0.1 mm), bent to an arc with the radius of 50 mm, was used as both contacting layer and electrode. The one end of SSF, 5 mm length, was fixed on the PTFE/Cu/PMMA structure. The actual maximum contacting length for arc-SSF is then 40 mm. Two wires were connected to SSF and copper film with the conjunctions winded by Kapton tape. A black rubber ring was used to bundle the device tightly, which can be used to adjust the length of SSF.

Fabrication of Multiple States Keyboard: An 85 mm × 85 mm × 3.5 mm acrylic board was used as the substrate. The nine identical EB-TENGs were fabricated on the acrylic board, and the whole fabricated processes were similar to the above section. The arc-SSFs (width of 6.5 mm, arc length of 20 mm, thickness of 0.1 mm, radius of 50 mm) were used. One end of the SSF, 4 mm length, was fixed, so the actual maximum contacting length is 16 mm.

Characterization: The electric measurement was conducted by a Keithley 6514 system electrometer. A software platform programmed using LabVIEW to achieve real-time data acquisition and analysis. A commercial linear mechanical motor was used to precisely adjust the separated distance between PTFE and SSF. A commercial analytical balance was used as a force sensor (OHAUS, PA224C), with readability 1×10^{-4} g. The actual force applied was calculated by the following formula, $F = mg$, where m is mass; g is gravitational acceleration, value adopted 9.8 m s^{-2}. The EB-TENG was put on the analytical balance and the SSF was pressed by linear mechanical motor in the experiments. In order to collect signal of acceleration sensor, two copper electrodes were glued beneath the disk, which respectively connected to the two terminals of EB-TENG, as shown in Figure 3d,e. Then two electric brushes contacted the electrodes, respectively. The electrometer collected the data by two leads connecting to the electric brushes. The vibrator was based on a commercial multimedia speaker system (MPC, MMP001176-01). The signals with different frequencies were input into the vibrator through a computer. The input music is part of "Georgia Tech (GT) fight song".

Finite Element Analysis: The FEA is carried out by utilizing the COMSOL software 5.2a. The potential distribution was calculated at different states under the open-circuit condition. It should be emphasized that the simulations in previous reports applied ideal average charge density ($\approx 10^{-4}$ cm^{-2}) without considering the real micromorphology.[37,38] Here, it is thought that the tested voltage results can also be the reference criterion for the selection of average charge density. The 5×10^{-8} cm^{-2} was adopted in our simulation. The simulation of eigenfrequency was conducted for each different length of SSF (40–1 mm). The whole SSF was set at free state except one of the ends was constrained.

Supporting Information

Supporting Information is available from the Wiley Online Library or from the author.

Acknowledgements

Conflict of Interest

The authors declare no conflict of interest.

Keywords

[1] Z. L. Wang, *Mater. Today* **2017**, *20*, 74.
[2] Z. L. Wang, J. Chen, L. Lin, *Energy Environ. Sci.* **2015**, *8*, 2250.
[3] S. Wang, L. Lin, Z. L. Wang, *Nano Energy* **2015**, *11*, 436.
[4] F.-R. Fan, Z.-Q. Tian, Z. L. Wang, *Nano Energy* **2012**, *1*, 328.
[5] S. L. Zhang, M. Xu, C. Zhang, Y.-C. Wang, H. Zou, X. He, Z. Wang, Z. L. Wang, *Nano Energy* **2018**, *48*, 421.
[6] J. Wang, S. Li, F. Yi, Y. Zi, J. Lin, X. Wang, Y. Xu, Z. L. Wang, *Nat. Commun.* **2016**, *7*, 12744.
[7] M. Xu, Y.-C. Wang, S. L. Zhang, W. Ding, J. Cheng, X. He, P. Zhang, Z. Wang, X. Pan, Z. L. Wang, *Extreme Mech. Lett.* **2017**, *15*, 122.
[8] J. Bae, J. Lee, S. Kim, J. Ha, B. S. Lee, Y. Park, C. Choong, J. B. Kim, Z. L. Wang, H. Y. Kim, J. J. Park, U. I. Chung, *Nat. Commun.* **2014**, *5*, 4929.
[9] Z. H. Lin, G. Cheng, S. Lee, K. C. Pradel, Z. L. Wang, *Adv. Mater.* **2014**, *26*, 4690.
[10] K. Dong, J. Deng, Y. Zi, Y. C. Wang, C. Xu, H. Zou, W. Ding, Y. Dai, B. Gu, B. Sun, Z. L. Wang, *Adv. Mater.* **2017**, *29*, 1702648.
[11] J. Chen, G. Zhu, W. Yang, Q. Jing, P. Bai, Y. Yang, T. C. Hou, Z. L. Wang, *Adv. Mater.* **2013**, *25*, 6094.
[12] M. Xu, P. Wang, Y.-C. Wang, S. L. Zhang, A. C. Wang, C. Zhang, Z. Wang, X. Pan, Z. L. Wang, *Adv. Energy Mater.* **2018**, *8*, 1702432.
[13] J. Wang, W. Ding, L. Pan, C. Wu, H. Yu, L. Yang, R. Liao, Z. L. Wang, *ACS Nano* **2018**, *12*, 3954.
[14] P. K. Yang, L. Lin, F. Yi, X. Li, K. C. Pradel, Y. Zi, C. I. Wu, J. H. He, Y. Zhang, Z. L. Wang, *Adv. Mater.* **2015**, *27*, 3817.
[15] J. Yang, J. Chen, Y. Su, Q. Jing, Z. Li, F. Yi, X. Wen, Z. Wang, Z. L. Wang, *Adv. Mater.* **2015**, *27*, 1316.
[16] Z. L. Wang, *Faraday Discuss.* **2014**, *176*, 447.
[17] S. Niu, S. Wang, Y. Liu, Y. S. Zhou, L. Lin, Y. Hu, K. C. Pradel, Z. L. Wang, *Energy Environ. Sci.* **2014**, *7*, 2339.
[18] S. Niu, S. Wang, L. Lin, Y. Liu, Y. S. Zhou, Y. Hu, Z. L. Wang, *Energy Environ. Sci.* **2013**, *6*, 3576.
[19] R. D. I. G. Dharmasena, K. D. G. I. Jayawardena, C. A. Mills, J. H. B. Deane, J. V. Anguita, R. A. Dorey, S. R. P. Silva, *Energy Environ. Sci.* **2017**, *10*, 1801.
[20] S. Niu, Y. Liu, S. Wang, L. Lin, Y. S. Zhou, Y. Hu, Z. L. Wang, *Adv. Mater.* **2013**, *25*, 6184.
[21] C. Xu, Y. Zi, A. C. Wang, H. Zou, Y. Dai, X. He, P. Wang, Y. C. Wang, P. Feng, D. Li, Z. L. Wang, *Adv. Mater.* **2018**, *30*, 1706790.
[22] M. Sow, D. J. Lacks, R. M. Sankaran, *J. Electrost.* **2013**, *71*, 396.
[23] S. Wang, L. Lin, Y. Xie, Q. Jing, S. Niu, Z. L. Wang, *Nano Lett.* **2013**, *13*, 2226.
[24] L. Lin, S. Wang, S. Niu, C. Liu, Y. Xie, Z. L. Wang, *ACS Appl. Mater. Interfaces* **2014**, *6*, 3031.
[25] L. Lin, S. Wang, Y. Xie, Q. Jing, S. Niu, Y. Hu, Z. L. Wang, *Nano Lett.* **2013**, *13*, 2916.
[26] L. Xu, T. Z. Bu, X. D. Yang, C. Zhang, Z. L. Wang, *Nano Energy* **2018**, *49*, 625.
[27] L. Lin, Q. Jing, Y. Zhang, Y. Hu, S. Wang, Y. Bando, R. P. S. Han, Z. L. Wang, *Energy Environ. Sci.* **2013**, *6*, 1164.
[28] C. Wu, C. Ding, R. Liu, J. Wang, A. C. Wang, J. Wang, S. Li, Y. Zi, Z. L. Wang, *Mater. Today* **2018**, *21*, 216.
[29] M. Ma, Q. Liao, G. Zhang, Z. Zhang, Q. Liang, Y. Zhang, *Adv. Funct. Mater.* **2015**, *25*, 6489.
[30] A. F. Diaz, R. M. Felix-Navarro, *J. Electrost.* **2004**, *62*, 277.
[31] M. M. Apodaca, P. J. Wesson, K. J. Bishop, M. A. Ratner, B. A. Grzybowski, *Angew. Chem., Int. Ed.* **2010**, *49*, 946.
[32] S. Niu, Y. Liu, S. Wang, L. Lin, Y. S. Zhou, Y. Hu, Z. L. Wang, *Adv. Funct. Mater.* **2014**, *24*, 3332.
[33] S. M. Han, H. Benaroya, T. Wei, *J. Sound Vib.* **1999**, *225*, 935.
[34] M. L. Ali, J. V. Monaco, C. C. Tappert, M. Qiu, *J. Signal Process. Syst.* **2016**, *86*, 175.
[35] S. P. Banerjee, D. Woodard, *J. Pattern Recognit. Res.* **2012**, *7*, 116.
[36] F. Monrose, A. D. Rubin, *Future Gener. Comput. Syst.* **2000**, *16*, 351.
[37] J. Wang, C. Wu, Y. Dai, Z. Zhao, A. Wang, T. Zhang, Z. L. Wang, *Nat. Commun.* **2017**, *8*, 88.
[38] J. Chun, B. U. Ye, J. W. Lee, D. Choi, C. Y. Kang, S. W. Kim, Z. L. Wang, J. M. Baik, *Nat. Commun.* **2016**, *7*, 12985.